Navier-Stokes Solution to the Flowfield Over Ice Accretion Shapes

J. N. Scott,* W. L. Hankey,† F. J. Giessler,‡ and T. P. Gielda§
University of Dayton Research Institute, Dayton, Ohio

The numerical simulation of flow about ice accretion shapes has been accomplished by solving the Navier-Stokes equations using MacCormack's explicit finite-difference scheme. The computations were performed on a vector processor computer. The influence of turbulence is taken into account by means of an algebraic eddy-viscosity model. In order to optimize the grid spacing and to achieve near orthogonality at the surface of the complex ice shapes, a hyperbolic grid generation scheme is utilized. Particular attention is given to the heat-transfer process for which good agreement between the numerical and experimental results is achieved. In addition, liquid water droplet trajectories are computed within the flowfield along with the resulting impingement efficiencies using a parabolized Navier-Stokes formulation.

Nomenclature

A = area
C_D = drag coefficient of droplet
d = droplet diameter
f = drag of droplet/unit mass
g = gravity acceleration
h = heat transfer coefficient
J = Jacobian of transformation
k = thermal conductivity
m = droplet mass
n = surface outer normal
Nu = Nusselt number
p = pressure
$\dot{q}$ = heat transfer rate
Re_d = Reynolds number for droplet
S = frontal area of droplet
T = temperature
t = time
V = velocity of air
V_p = velocity of droplet
$x\text{-}y$ = Cartesian coordinates
β = local impingement efficiency
μ = viscosity of air
$\zeta\text{-}\eta$ = coordinates in computational plane
ρ = air density
ρ_p = liquid water content
ρ_w = water density
$\underline{\underline{\tau}}$ = stress tensor

Introduction

THE national interest in aircraft icing receded in the 1950's due to the introduction of the jet engine (with its higher cruise altitude) and radar. Interest has recently returned to this area for both military and civilian aviation.

The condition of ice accretion arises when an aircraft encounters a metastable cloud containing supercooled liquid droplets. Two different classes of icing have been identified: rime and glaze. Rime ice occurs at low temperatures (below 10°F) when ice forms immediately upon droplet impact. The

*Associate Professor. Associate Fellow AIAA.
†Consultant. Associate Fellow AIAA.
‡Research Engineer. Member AIAA.
§Associate Research Engineer. Member AIAA.

convection process is sufficient for the air to remove the high latent heat of fusion of the droplets that are changing phase from liquid to solid. The accreted shape on the airfoil, therefore, resembles the impingement efficiency distribution profile. Glaze ice occurs at a higher temperature (25–32°F) and is formed when droplets run a certain distance from the point of impact before freezing. Glaze is the worst situation in that a liquid-ice mixture flows over the leading edge of an airfoil and forms ice "horns." These protrusions act as spoilers that increase drag and decrease lift.

The aerothermodynamic phenomenon at the surface is one of the most complex encountered in fluid mechanics.[1] The interface experiences energy exchange due to kinetic energy from droplet impact, heat transfer by convection and phase change, enthalpy differences in the air, water and ice flows, and mass transfer by evaporation (Fig. 1).

To date, analytical studies have failed to provide techniques that accurately predict the ice accretion rates encountered in icing tunnels. However, within the past few years a tool has been developed that has the potential for simulating the icing process. This tool lies in the numerical solution of the time-dependent Navier-Stokes equations.[2] The dynamic equations of the water droplets are added to these equations for the air flow and simultaneously solved to simulate ice accretion.

Technical Approach

It is desirable to develop a computer program that will possess the capability to solve the complete icing process involving the air-droplet mixture with phase change on the surface. This flowfield program would also include the computation of the aerodynamic lift and drag, heat-transfer distribution, droplet impingement efficiency, etc. The present approach develops the overall strategy to achieve these goals.

The first issue to address is the unsteady nature of the phenomenon. Although the ice shape configuration changes with time, the rate of growth is slow (10^{-4} ft/s) compared to the flight speed (200 ft/s); therefore, a quasisteady analysis is appropriate. This approach involves computation of Navier-Stokes solutions for a sequence of shapes starting from the original configuration, computing the growth rate, advancing the configuration over a fixed time interval recomputing a new growth rate, etc., until the final shape is attained.

A primary element of this approach is the accurate computation of the heat transfer over a roughened surface of complex geometry. A series of experimental heat-transfer test results[3-6] are used to assist in the validation of the computational fluid dynamic (CFD) methods. (Thus, the numerical approach is used to compute the flowfield about these ice shapes with resultant heat transfer.)

The configurations computed are models of ice accretion shapes formed on a circular cylinder in the NASA Lewis Icing Research Tunnel (IRT). These shapes are for 2, 5, and 15-min models of glaze ice and a 15-min accumulation of rime ice. An existing Navier-Stokes program was modified to compute the flowfield over these four shapes.

Governing Equations

The governing equations are obtained by adding body forces to the Navier-Stokes equations to account for the drag of the water droplets and surface roughness. In addition, a continuity and momentum equation is required to develop the trajectory equations for the droplets.

Air equations:

$$\frac{\partial \rho}{\partial t} + \nabla \cdot \rho V = 0$$

$$\rho \frac{DV}{Dt} = \nabla \cdot \underline{\underline{\tau}} - \rho_p f$$

$$\rho \frac{De}{Dt} = \nabla \cdot (\underline{\underline{t}} \cdot V + \dot{q}) - \rho_p f \cdot V$$

Water droplet equations:

$$\frac{\partial \rho_p}{\partial t} + \nabla \cdot \rho_p V_p = 0$$

$$\frac{\partial V_p}{\partial t} + V_p \cdot \nabla V_p = g + f$$

where

$$f = \frac{C_D \rho S}{2m} |V - V_p|(V - V_p) = \text{droplet drag/unit mass}$$

The water droplets are assumed to be uniform spheres of diameter d. Cloud physics experiments indicate that the diameter varies between 5 and 50 μ depending on the air temperature and liquid water content.[7] Often an average diameter of 20 μ is used in ice accretion studies. Therefore,

$$\frac{\rho S}{2m} = \frac{\rho \pi d^2/4}{2\rho_w \pi d^3/6} = \frac{3\rho}{4\rho_w d}$$

and the drag coefficient depends on the Reynolds number[8]

$$C_D = C_D(Re_d)$$

A curve fit of this classic plot produces the following relationships:[9]

$$Re_d < 1 \quad C_D = \frac{24}{Re_d} \text{ (Stokes flow)}$$

$$1 < Re_d < 400 \quad C_D = \frac{24}{(Re_d)0.646}$$

$$400 < Re_d < 3 \times 10^5, \qquad C_D = 0.5$$

These values are used in the computation of the water droplet trajectories.

Grid Generation

The grid was developed using the hyperbolic grid generation scheme of Steger and Sorenson.[10] This technique appears ideally suited for computing grids for the irregular shapes of ice configurations. This method first requires a detailed description of the surface geometry. The program produces an orthogonal, body-oriented grid (that is preferable in CFD computations) and clusters the grid points near the surface. The hyperbolic method has little control over the final exterior
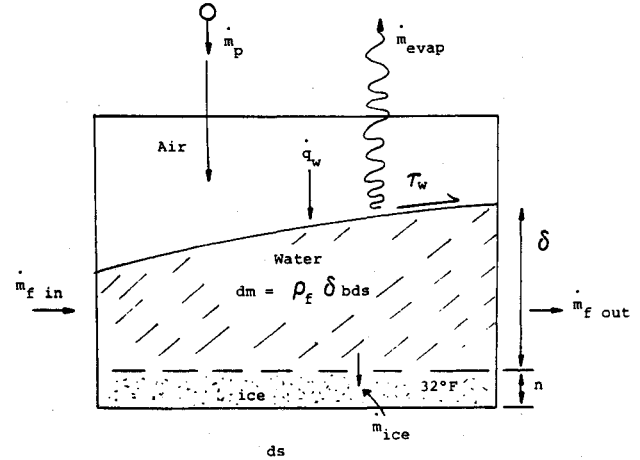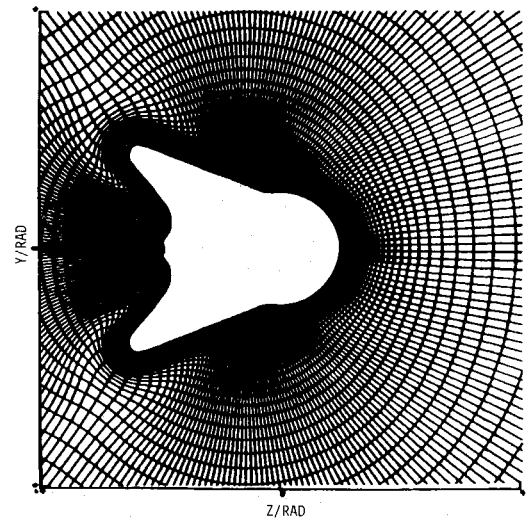

Fig. 1   Sketch of interface phenomena.

15 minute glaze ice
    1 degree increment on glaze portion, 3 degrees on cylinder
    60 radial steps

Fig. 2   Fifteen-minute glaze grid.

grid shape, which is perfectly acceptable for external flow problem (but unacceptable for internal flows). An example grid for a typical ice shape is shown in Fig. 2.

Boundary Conditions

Far Field

At the far field boundary, the following conditions are prescribed:

$$V_\infty, T_\infty, P_\infty$$

$$\rho_p = \text{LWC} = \text{liquid water content of cloud}$$

$$V_p = V_\infty$$

Surface

At the surface, the following conditions prevail:

$$V = 0, \qquad T_W \text{ specified}, \qquad \frac{\partial p}{\partial n} = 0$$

Turbulence Model

The turbulence is simulated by the algebraic eddy-viscosity model developed by Baldwin and Lomax.[11] This turbulence

model is incorporated into the computational procedure near the surface. The procedure used for the present calculations assumes the presence of two layers. The Prandtl-van Driest formulation is used for the inner layer:

$$\varepsilon_i = \rho \ell^2 |\omega|$$

where

$$\ell = ky\left[1 - \exp\left(\frac{-y^+}{A^+}\right)\right]$$

The magnitude of the vorticity $|\omega|$ is:

$$|\omega| = \left|\frac{\partial u}{\partial y} - \frac{\partial v}{\partial x}\right|$$

$$y^+ = \left[\frac{\rho_w |\omega_w|}{\mu_w}\right]^{\frac{1}{2}} y$$

The distance normal to the surface is y, $A^+ = 26$ is the sublayer thickness, $k = 0.40$ is the von Karman constant, and the subscript w denotes values at the surface.

The model switches from the van Driest formulation to the formulation for the outer region at the smallest value of y for which the inner and outer values of the eddy-viscosity are equal (i.e., $\varepsilon_i \geq \varepsilon_0$). The formulation for the outer layer is given by

$$\varepsilon_0 = \rho K C_{cp} F_{\max} y_{\max} F_{KLEB}$$

where

$$F_{\max} = y_{\max} |\omega| \left[1 - \exp\left(\frac{-y^+}{A^+}\right)\right]$$

The value of y at which $F_{\max}$ occurs is $y_{\max}$.

$$F_{KLEB} = [1 + 5.5(C_{KLEB} y / y_{\max})^6]^{-1}$$

$$K = 0.0168, \qquad C_{cp} = 1.6, \qquad C_{KLEB} = 0.3$$

Solution of the Water Droplet Equations

In the past, droplet trajectory equations have been solved using the Lagrangian method. In this investigation an Eulerian method was used for two reasons: first, to make the droplet system of equations compatible with the airflow equations and, second, to include the variation of the liquid water content (ρ_p) throughout the flowfield.

The droplet equations are similar in form to the airflow equations with the exception that the stress tensor is zero. This difference, however, changes the mathematical character of the partial differential equations from elliptic to hyperbolic. This means that the hyperbolic equations may be marched in space using a modified Parabolized Navier-Stokes code (PNS).[12]

To apply a space-marching technique correctly, the eigenvalues of the governing equations must be real (indicating the character of the equations is hyperbolic).

The governing equations in divergence form are written as

$$E_x + F_y = H$$

where, E, F, and H are defined by

$$E = \begin{vmatrix} \rho u \\ \rho u^2 \\ \rho uv \end{vmatrix} \qquad F = \begin{vmatrix} \rho v \\ \rho uv \\ \rho v^2 \end{vmatrix} \qquad H = \begin{vmatrix} 0 \\ -fx \\ -fy \end{vmatrix}$$

In order to perform the eigenvalue analysis,[13] the E and F vectors are factored such that

$$E_x = \frac{\partial E}{\partial U} U_x = A U_x$$

$$F_y = \frac{\partial F}{\partial U} U_y = B U_x$$

where

$$U = \begin{vmatrix} \rho \\ u \\ v \end{vmatrix}$$

The A and B matrices are found to be

$$A = \begin{vmatrix} u & \rho & 0 \\ 0 & \rho u & 0 \\ 0 & 0 & \rho u \end{vmatrix}$$

$$B = \begin{vmatrix} v & 0 & 0 \\ 0 & \rho v & 0 \\ 0 & 0 & \rho v \end{vmatrix}$$

Applying the above factorization, the governing equation can be rewritten as

$$U_x + A^{-1} B U_y = A^{-1} H$$

To determine the character of this equation set it is necessary to find the eigenvalues of the matrix $A^{-1}B$, which was found to be

$$A^{-1}B = \begin{vmatrix} \dfrac{v}{u} & \dfrac{-\rho v}{u^2} & \dfrac{\rho}{u} \\ 0 & \dfrac{v}{u} & 0 \\ 0 & 0 & \dfrac{v}{u} \end{vmatrix}$$

The characteristic equation of the matrix $A^{-1}B$ is determined from

$$\det[A^{-1}B - \lambda I] = 0$$

or in simplified form

$$\left(\frac{v}{u} - \lambda\right)^3 = 0$$

The eigenvalues of the matrix $A^{-1}B$ are defined as the roots of the characteristic equation. Therefore, the eigenvalues of $A^{-1}B$ are

$$\lambda = \frac{v}{u}$$

Since the eigenvalues are real, the character of the governing fluid dynamic equations is hyperbolic. Therefore, the governing equations can be solved with a hyperbolic space-marching scheme.

Solution Procedure

The airflow was computed using a well documented Navier-Stokes code adapted from the original program developed by Shang.[14] The MacCormack finite-difference algorithm is utilized and the program is optimized for a vector processor.[15] Also, the hyperbolic grid generator of Steger and Sorenson[10] is used as discussed previously.

The computation of the droplet trajectories is computed using technology developed for the PNS-solving schemes. As noted before, the droplet equations are hyperbolic since the stress-tensor vanishes for this model. (No collisions between

droplets are considered in the formulation and, hence, no pressure or shear terms are present.) The governing equations are transformed into a ξ-η computational domain and take on the following form:

$$\begin{vmatrix} \rho_p V \\ \rho_p u_p V \\ \rho_p v_p V \end{vmatrix}_\eta = \begin{vmatrix} 0 \\ \dfrac{\rho_p(u_p - u)}{\tau J} \\ \dfrac{\rho_p(\omega_p - v)}{\tau J} \end{vmatrix} - \begin{vmatrix} \rho_p U \\ \rho_p u_p U \\ \rho_p v_p U \end{vmatrix}_\xi$$

where the contravariant velocity components are represented as

$$U = y_\eta u_p - x_\eta v_p$$

$$V = x_\xi v_p - y_\xi u_p$$

$$J^{-1} = \begin{vmatrix} x_\xi & x_\eta \\ y_\xi & y_\eta \end{vmatrix} \qquad \tau = \frac{4\rho_w d^2}{3 C_D Re_d \mu}$$

The upstream boundary conditions are:

$$\rho_p(\infty) = \text{LWC}$$

$$u_p(\infty) = V_\infty$$

$$v_p(\infty) = 0$$

Given the air velocity components (u,v) from the solution of the airflow equations, the droplet equations are marched in the η direction inward toward the body. After attaining the body surface, the values of u_p, v_p, and ρ_p are recorded from which the local impingement efficiency β may be determined.

Local Impingement Efficiency

The impingement efficiency of an icing shape is a measure of its ability to intercept incoming droplets.[7] The impingement efficiency β at any point is the ratio of the actual mass flux of droplets impacting that point divided by the freestream incoming mass flux of droplets. Equivating mass fluxes produces a relationship for β:

$$\beta(\text{LWC}) V_\infty dy = (\rho_p V_p \cdot ndA)_w$$

where

$$V_p = iu_p + jv_p$$

$$ndA = idy - jdx$$

Thus

$$\beta = \left(\frac{\rho_p}{\text{LWC}}\right)_w \left[\frac{u_p\, dy - v_p\, dx}{V_\infty dy}\right]_w$$

But

$$\frac{dy}{dx} = \tan\theta$$

hence

$$\beta = \left(\frac{\rho_p}{\text{LWC}}\right)_w \left[\frac{u_p - v_p \cot\theta}{V_\infty}\right]_w$$

A dimensional analysis of the water droplet equations indicate that the impingement efficiency is a function of the geometry and only one flow parameter K_o where

$$K_o = \frac{V_\infty \tau}{D}$$

This single parameter is a type of Reynolds number, taking into account all flow variables of the problem, and is very useful for evaluating impingement efficiencies. This term is the inertia parameter defined by Langmuir and Blodgett[16] in their work on water droplet trajectories.

Nusselt Number

A primary concern is the heat-transfer coefficient at the surface. This value will determine the cooling rate that is the key to predicting ice accretion. The experimental heat-transfer data is expressed in terms of local Nusselt number.

$$Nu = \frac{hD}{k}$$

where

$$\dot{q}_w = k\left(\frac{\partial T}{\partial n}\right)_w = h(T_t - T_w)$$

Therefore

$$Nu = \frac{D\left(\dfrac{\partial T}{\partial n}\right)_w}{(T_t - T_w)}$$

Results

To assess the validity of the numerical simulation, the heat-transfer distribution over a smooth circular cylinder under laminar flow conditions was computed. The numerical results for the Nusselt number are compared with the exact solution obtained by Frossling[17] in Fig. 3. This case is for a Reynolds number of $Re_d = 138,000$, and a cylinder diameter of 2 in. The excellent agreement observed establishes the validity of the numerical approach.

Computations were then carried out for the four specified ice shapes. Results were first obtained using a grid consisting of 60 points in the radial direction and 60 points in the circumferential direction. For this configuration the circumferential grid point spacing was in increments of 3 deg from the origin of the cylinder. Although these results exhibited the proper trends, they did not provide the desired accuracy. Thus, in an effort to improve the accuracy, grid refinement was incorporated into the upstream quadrant of the computational domain. This was accomplished by reducing the circumferential grid spacing to increments of 0.5 deg. This resulted in excellent agreement between the computed flowfield and experimental data.

As noted previously, one of the important aspects of the ice accretion phenomena is the heat-transfer process. Hence, the
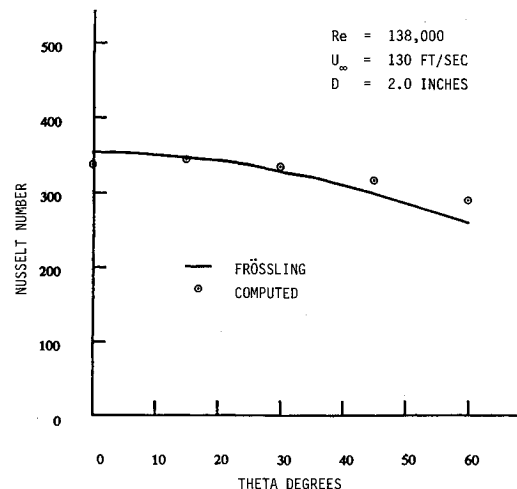

Fig. 3 Comparison of Frossling solution and computation of Nusselt number.

computed Nusselt number is compared with the experimental data of Van Fossen et al.[3] for the four prescribed ice shapes, i.e., 2, 5, and 15-min glaze and 15-min rime ice cases. The computed Nusselt number for the 15-min glaze ice shape gives excellent agreement with experimental data from the stagnation point to approximately 35 deg (Fig. 4). This point corresponds to the peak or tip of the ice horn. Beyond this point a region of separated flow develops and, as a result of the oscillatory nature of the separation, large fluctuations in the instantaneous value of the Nusselt number are observed. The exact solution for Nusselt number over a circular cylinder is also shown in Fig. 4 for reference purposes. The features of the separation are also apparent upon examining the velocity vectors for the computed flowfield. Figure 5 shows the velocity vectors for the 15-min glaze shape at two different times. The large region of separated flow appears just beyond the tip of the horn (Fig. 5a). This recirculation region stretches and moves downstream with increasing time (Fig. 5b). The temperature at one grid point off the surface is shown in Fig. 6. The fluctuation in the temperature downstream at the tip of the ice shape can be attributed to the unsteady nature of the separated flow in this region.

Similar features are observed for the 2- and 5-min glaze ice shapes, although to a lesser degree than for the 15-min glaze. In analyzing the Nusselt number for these cases, it has been observed that there is a large amount of scatter in the experimental data[3]; however, this comparison of the general trends (especially in the vicinity of the stagnation point and the tip of the ice horn) is in good agreement. The data comparison for the Nusselt number for the 2- and 5-min glaze configurations are shown in Figs. 7 and 8, respectively. The velocity vectors for the 5-min case are shown in Fig. 9. The figure reveals how the region of flow separation depends on the size of the ice horn shape. In the case of the 2-min glaze, the size of the ice is still quite small and has virtually no horn associated with it. Hence, there is very little separation present. For the 5-min glaze ice shape, a discernible horn has started to form and the region of separated flow has become quite visible, thus showing the growth progression toward the 15-min glaze shape.

The flow characteristics about the 15-min rime ice shape are quite different. Figure 10 shows the velocity vectors for this shape and indicates that no flow separation is present. The

computed Nusselt number for this shape shows a peak near the tip that appears to coincide with the experimental results (Fig. 11).

Figure 12 shows the computed path lines for water droplets for 10-m-diam flowing around a 2-in.-diam cylinder in
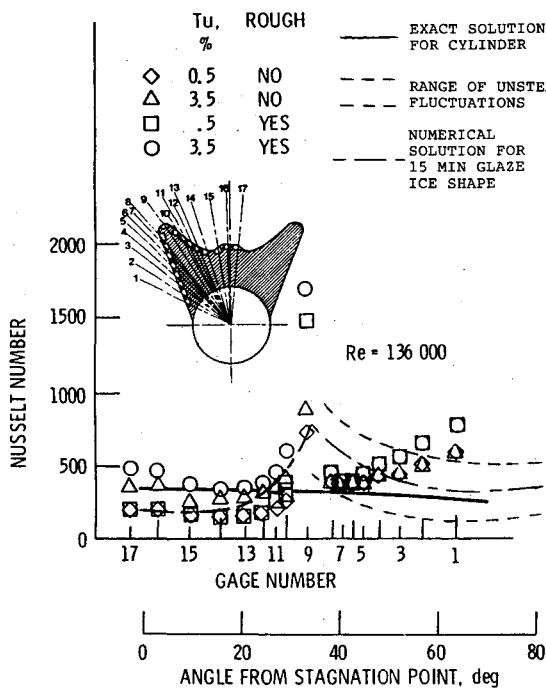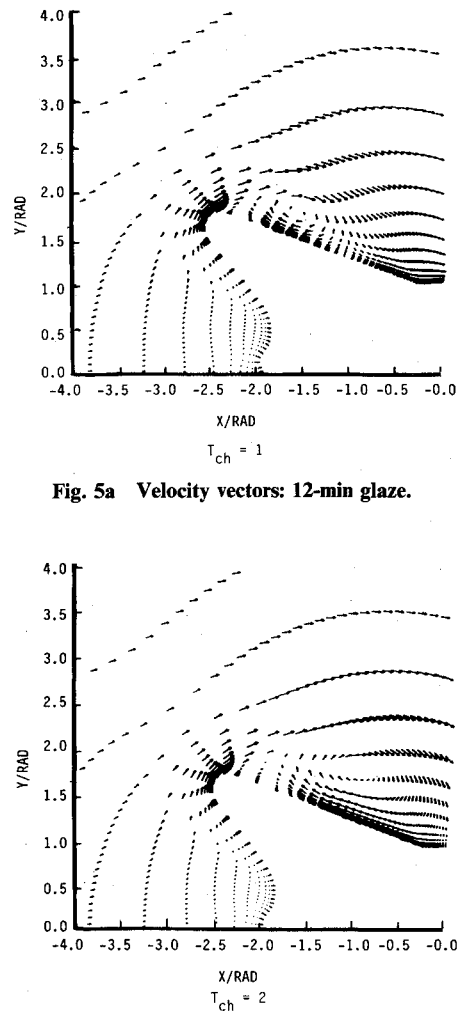

Fig. 5a   Velocity vectors: 12-min glaze.

Fig. 5b   Velocity vectors: 12-min glaze.

Fig. 4   Computed Nusselt number for 15-min glaze.
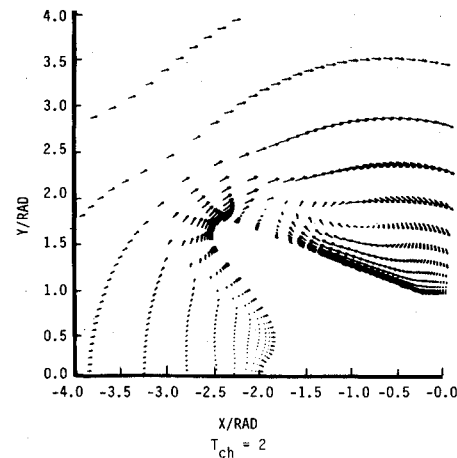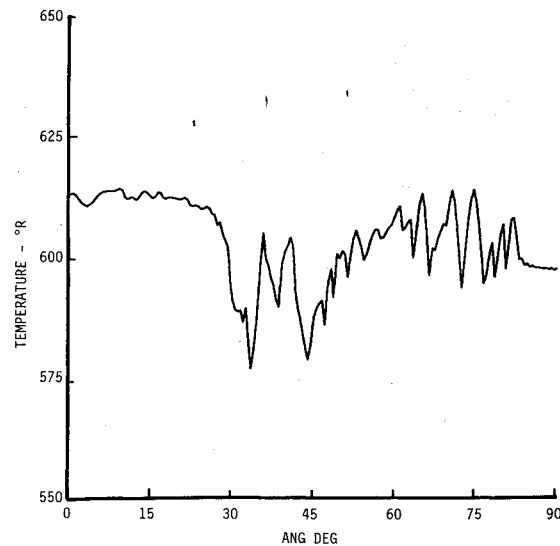

Fig. 6   Temperature vs angle: 15-min glaze.

Fig. 7   Nusselt number for 2-min glaze.

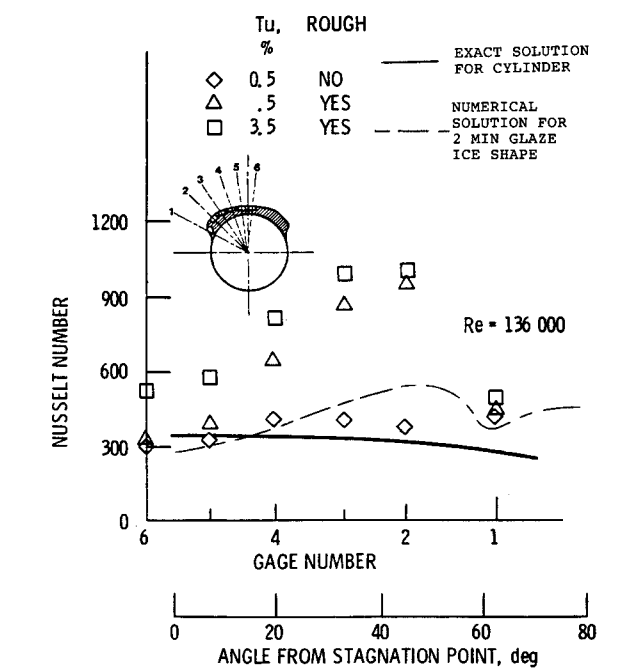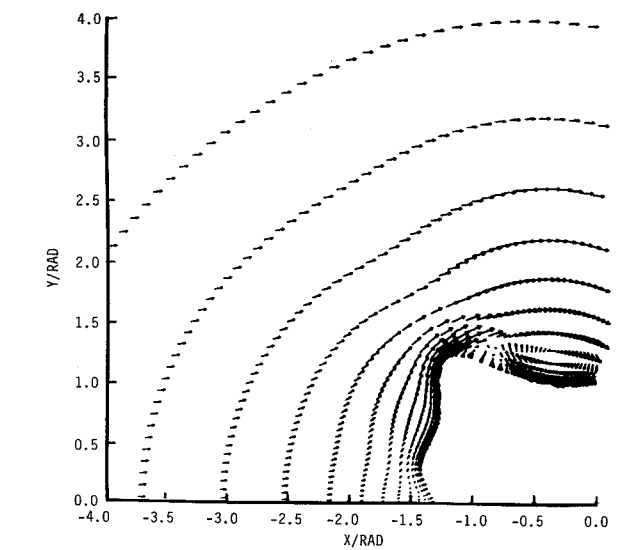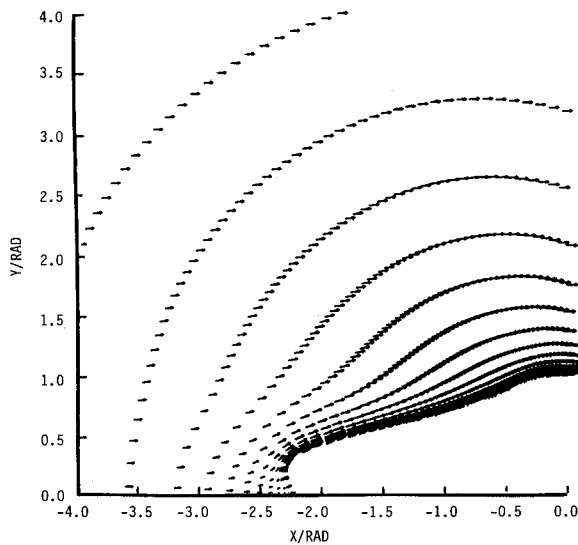Fig. 10   Velocity vector for the 15-min rime.

Fig. 8   Nusselt number for 5-min glaze.

Fig. 11   Nusselt number for 15-min rime.

Fig. 9   Velocity vectors for the 5-min glaze.
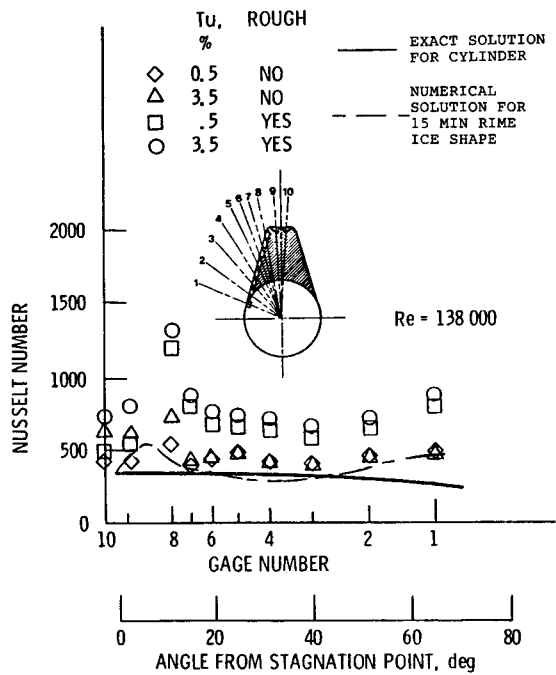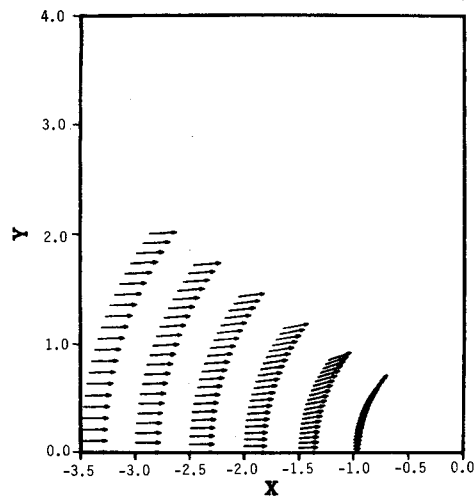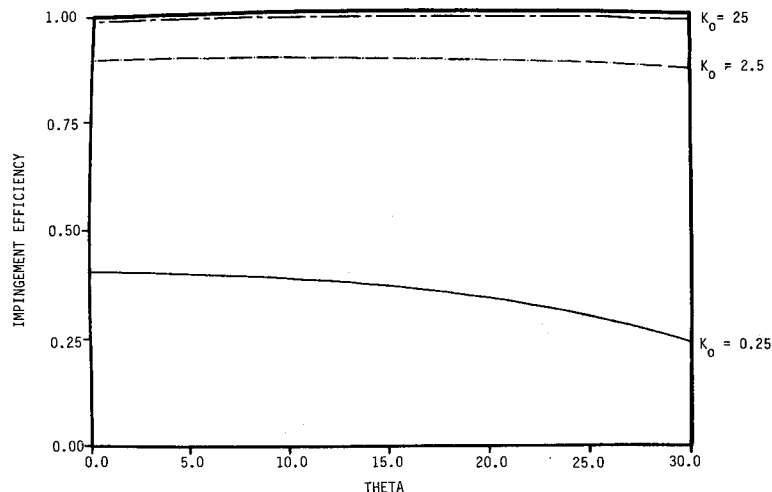

Fig. 12   Droplet trajectories.

Fig. 13   Impingement efficiency.

potential flow with a freestream velocity of 130 fps ($K_o = 0.476$). Figure 13 depicts the computed impingement efficiency for several values of K_o.

Summary

An analysis of the flowfield, composed of air with small water droplets, encountered during ice accretion of cylinders has been accomplished. The method utilizes the numerical solution of the Navier-Stokes equation to predict the airflow over complex ice geometries.

A marching code, based on the parabolized Navier-Stokes formulation, is used to compute the water droplet trajectories and resulting droplet impingement efficiencies. Good agreement is obtained with the experimental heat-transfer distributions for a series of ice shapes.

Acknowledgment

References

[1]Shaw, R. J., "Progress Toward the Development of an Aircraft Icing Analysis Capability," NASA TM-83562, Jan. 1984.

[2]Potapczuk, M. G. and Gerhart, P. M., "Progress in Development of a Navier-Stokes Solver for Evaluation of Iced Airfoil Performance," AIAA Paper 85-0410, Jan. 1985.

[3]Van Fossen, G. J., Simoneau, R. J., Olsen, W. A., and Shaw, R. J., "Heat Transfer Distributions around Nominal Ice Accretion Shapes Formed on a Cylinder in the NASA Lewis Icing Research Tunnel," AIAA Paper 84-0017, Jan. 1984.

[4]Pais, M. and Singh, S. N., "Determination of the Local Heat Transfer Coefficients of Three Simulated Smooth Ice Formation Characteristics on a Cylinder," AIAA Paper, 85-1836, Aug. 1985.

[5]Smith, M. E., Arimilli, R. V., and Keshock, E. G., "Measurement of Local Convective Heat Transfer Coefficients of Four Ice Accretion Shapes," NASA CR-174680, May 1984.

[6]Bragg, M. B. and Coirier, W. J., "Detailed Measurements of the Flow Field in the Vicinity of an Airfoil with Glaze Ice," AIAA Paper 85-0409, Jan. 1985.

[7]"Aircraft Icing," Workshop Proceedings, NASA CP-2086, Cleveland, Ohio, 1978.

[8]Schlichting, H., Boundary Layer Theory, 6th ed., McGraw-Hill, New York, 1968.

[9]Chow, C. Y., An Introduction to Computational Fluid Mechanics, Wiley, New York, 1979, p. 7.

[10]Steger, J. L. and Sorenson, R. L., "Use of Hyperbolic Partial Differential Equations to Generate Body Fitted Coordinates," Numerical Grid Generation Techniques, NASA CP 2166, 1980.

[11]Baldwin, B. S. and Lomax, H., "Thin Layer Approximation and Algebraic Model for Separated Turbulent Flows," AIAA Paper 78-257, Jan. 1978.

[12]Gielda, T. P. and McRae, D. S., "An Accurate, Stable, Explicit, Parbolized Navier-Stokes Solver for High Speed Flows," AIAA Paper 86-1116, Atlanta, GA, 1986.

[13]Vigneron, Y. C., Rakich, J. V., and Tannehill, J. C., "Calculation of Supersonic Viscous Flows over Delta Wings with Sharp Subsonic Leading Edges," AIAA Paper 78-1137, July 1978.

[14]Shang, J. S., "Oscillatory Compressible Flow Around a Cylinder," AIAA Paper 82-0098, Jan. 1982.

[15]Scott, J. N. and Hankey, W. L., "Numerical Simulation of Cold Flow in an Axisymmetric Centerbody Combustor," AIAA Journal, Vol. 23, May 1985, pp. 641–649.

[16]Langmuir, I. and Blodgett, K. B., "A Mathematical Investigation of Water Droplet Trajectories," Army Air Forces TR-5418, Feb. 1946.

[17]Frossling, N., "Evaporation, Heat Transfer, and Velocity Distribution in Two Dimensional and Rotationally Symmetrical Laminar Boundary-Layer Flow," NACA TM-1432, 1958.